Spin-dependent high-order topological states and corner modes in a monolayer FeSe/GdClO heterostructure

Qing Wang,[1,2] Rui Song,[3,1] and Ning Hao[1,*]

[1]*Anhui Key Laboratory of Condensed Matter Physics at Extreme Conditions, High Magnetic Field Laboratory, HFIPS, Chinese Academy of Sciences, Hefei, 230031, China*

[2]*Science Island Branch of Graduate School, University of Science and Technology of China, Hefei, Anhui 230026, China*

[3]*Science and Technology on Surface Physics and Chemistry Laboratory, Mianyang, Sichuan 621908, China*

(Received 31 October 2022; accepted 26 May 2023; published 9 June 2023)

We propose that a spin-dependent second-order topological insulator can be realized in a monolayer FeSe/GdClO heterostructure, in which substrate GdClO helps to stabilize and enhance the antiferromagnetic order in FeSe. The second-order topological insulator is free from spin-orbit coupling and in-plane magnetic field. We also find that two types of distinct corner modes residing in the intersections of two ferromagnetic edges and two antiferromagnetic edges exist. The underlying physics for the ferromagnetic corner mode follows a sublattice-chirality-kink picture. More interestingly, the ferromagnetic corner mode shows a spin-dependent property, which is also robust against spin-orbit coupling. Unexpectedly, the antiferromagnetic corner mode can be taken as a typical emergent and hierarchical phenomenon from an array of ferromagnetic corner modes. Remarkably, antiferromagnetic corner modes violate the general kink picture and can be understood as bound states of a one-dimensional Schrodinger equation under a connected potential well. Our findings not only provide a promising second-order topological insulator in electronic materials but also uncover some different properties of corner modes in high-order topological insulators.

DOI: 10.1103/PhysRevB.107.235406

I. INTRODUCTION

Recently, the high-order topological state (HOTS) has attracted intense interest in many fields of physics [1–12]. Among various HOTSs, the two-dimensional (2D) second-order topological insulator (SOTI) is the simplest one and is ideal for studying various new physics in HOTSs. To date, many experimentally feasible platforms have been shown to host SOTIs, mainly including photonic, phononic, acoustic, and microwave- and electrical-circuit artificial systems [13–19]. For electronic materials, in contrast, material platforms to realize SOTIs are very limited and just theoretically proposed in some carbon-based compounds such as graphdiyne, γ-graphyne, twisted bilayer graphene, and bismuth heterostructures [20–26]. However, none of the proposals have been experimentally realized. Furthermore, spinless or spin-polarized features of these proposals limit the exploration and study of the spin-dependent physics of 2D SOTIs. Therefore, it remains meaningful and urgent to explore experimentally feasible electronic materials hosting 2D SOTIs, in particular, the spin-dependent 2D SOTI.

Since superconductivity with ultrahigh transition temperature (>65 K) was discovered in monolayer FeSe/$SrTiO_3$ (FeSe/STO) [27], similar heterostructures, such as FeSe/Nb:$BaTiO_3$/$KTaO_3$, FeSe/MgO, FeSe/anatase TiO_2(001), and FeSe/$EuTiO_3$ [28–31], have attracted enormous interest in many research fields. In particular, research on monolayer FeSe/STO was extended to the field of topological physics in 2014 [32,33]. The subsequent theoretical work predicted that a long-range Néel antiferromagnetic (AFM) order can spontaneously form in monolayer FeSe/$SrTiO_3$ and a conventional topological insulator can arise by further taking into account spin-orbit coupling (SOC) [34]. However, the magnetism in monolayer FeSe/STO has not been settled [34–41].

In this work, we theoretically predict that a long-range Néel AFM order in monolayer FeSe can be stabilized and enhanced by introducing the ferromagnetic (FM) insulating substrate GdClO. This strategy can avoid the debate over magnetism in monolayer FeSe. The stability of the heterostructure is verified by self-consistent first-principles calculations. Once Néel AFM order is generated with the aid of a GdClO substrate, we find that a 2D SOTI naturally emerges and is free from SOC and in-plane magnetic field. Interestingly, the 2D SOTI hosts two types of distinct corner modes residing in the intersections of two FM edges and two AFM edges, respectively. FM corner modes can be intrinsic or extrinsic depending on whether the global or local crystalline symmetry of the four edge boundaries is enforced or not. Furthermore, FM corner modes can be understood by a sublattice-chirality-kink picture and show explicitly spin-dependent properties. This enables one to study spin physics of 2D SOTIs. Interestingly, AFM corner modes can be taken as emergent corner modes from an array of FM corner modes. This demonstrates an emergent and hierarchical phenomenon of physics in a very simple and explicit manner. Physically, they violate the general kink picture and correspond to the bound states of a one-dimensional Schrodinger equation under a connected potential well.

*haon@hmfl.ac.cn

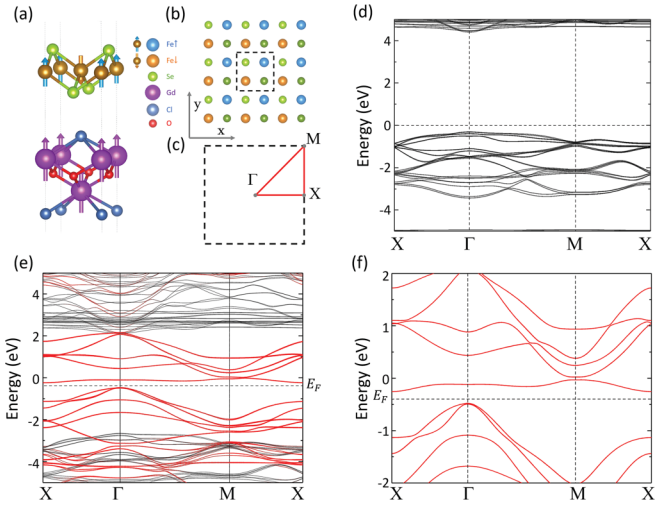

FIG. 1. (a) The spatial configuration of a monolayer FeSe/GdClO heterostructure and the stable magnetic structure from the first-principles calculations. (b) and (c) Lattice structure and Brillouin zone of Néel AFM FeSe. The dashed square in (b) labels the unit cell. (d) The band structure of FM GdClO with slab geometry. (e) The total band structure of a monolayer FeSe/GdClO heterostructure with the magnetic structure in (a). (f) The bands of freestanding monolayer FeSe assuming a Néel AFM order. The horizontal dashed lines labeled E_F in (c) and (d) denote the focused filling level.

II. THE FIRST-PRINCIPLES CALCULATION AND MODELING RESULTS

Inspired by the heterostructure of monolayer FeSe/STO, we believe that the natural cleavage surface of a promising substrate should be a square lattice with a matched lattice constant similar to that of FeSe. We note that the ready compound GdClO [42–46] fulfills such requirements due to its space group $P4/nmm$ symmetry and because its matched lattice constant is the same as that of FeSe. Figure 1(a) shows the configuration of a FeSe/GdClO heterostructure. It is well known that GdClO is a FM insulator with a very large gap of 5 eV, as shown in Fig. 1(d). The ferromagnetism is from Gd, with a magnetic moment of $7\mu_B$. Note that Gd atoms have double-layer structures, and only the top layer Gd atoms strongly couple to one sublattice of Fe square lattices through van der Waals (vdW) interaction. It is expected that sublattice A of Fe square lattices can generate ferromagnetism with the aid of the top layer of Gd. However, the magnetism of sublattice B of Fe square lattices cannot be intuitively determined. Thus, we perform a first-principles calculation to consider the magnetic configuration of the FeSe/GdClO heterostructure (see Appendixes A and B for details). Figure 1(a) shows the determined stable magnetic configuration. Interestingly, monolayer FeSe generates a stable long-range Néel AFM order on a FM substrate GdClO. Figure 1(e) gives the band structures of the FeSe/GdClO heterostructure. The electronic states are nearly decoupled between the FeSe monolayer and GdClO substrate due to weak vdW interaction and lack of charge transfer. Figure 1(f) gives the band structure of freestanding monolayer FeSe with an assumed Néel AFM order (also see Fig. 6 in Appendix B). It is the same as the FeSe part of the FeSe/GdClO heterostructure shown in Fig. 1(e). Note that some recent works focused on the small-gap regime near 0 eV at the M point in Fig. 1(f) and discussed possible 2D SOTSs induced by SOC and in-plane magnetic field [47,48]. In the following, we focus on the large-gap regime ~ 0.3 eV, labeled by E_F in Figs. 1(e) and 1(f), and explicitly demonstrate that a pristine 2D SOTS emerges and is free from SOC and in-plane magnetic field.

The bulk topology of such a pristine 2D SOTI can be characterized by both a topological invariant and a bulk quadrupole moment. From Fig. 1(b), monolayer Néel AFM FeSe has symmetries of $\hat{P}\hat{T}$, $\{\hat{C}_{2x}|1/2,0\}$, $\{\hat{C}_{4z}\hat{P}|0,1/2\}$, and $\{\hat{C}_{4z}\hat{T}|0,1/2\}$, with $\hat{P}$, $\hat{T}$, and $\{\hat{E}|1/2,0\}$ being the inversion, time-reversal, and fractional translation symmetries, respectively. The topological invariant characterizing the bulk topology of 2D SOTIs can be calculated with the method developed in the case of chiral HOTSs but limited to two dimensions [4]. Since the topological invariant depends only on the $\Gamma=(0,0)$ and $M=(\pi,\pi)$ points, where the representation of fractional translation symmetry $e^{ik_{x/y}/2}$ takes a value of 1 or i and is redundant, $(\hat{C}_{4z}\hat{P})^4=-1$, and the eigenvalues of $\hat{C}_{4z}\hat{P}$ are four roots of -1. Due to $[\hat{C}_{4z}\hat{P},\hat{P}\hat{T}]=0$ and $\hat{P}\hat{T}$ being antiunitary, they have to come in complex-conjugate pairs $\{\xi e^{i\pi/4},\xi e^{-i\pi/4}\}$, with $\xi=1$ or -1. The topological invariant can be defined as

$$(-1)^{v_c}=\prod_{n=1}^{N/2}\xi_{n,\Gamma}\xi_{n,M}. \tag{1}$$

Here, N labels the number of filled bands. Monolayer Néel AFM FeSe has 22 occupied bands, and the 11 calculated ξ values at Γ/M points are $\xi_{(1,\ldots,11),\Gamma/M}=(\pm1,-1,\pm1,\mp1,\mp1,1,-1,1,\mp1,\mp1,\pm1)$. This yields $v_c=1$, explicitly confirming a 2D SOTI. In the pioneering work on HOTSs [1,2], high-order topology was also understood from the change in the bulk charge dipole moment $p_{x/y}$ and quadrupole moment q_{xy}, which are defined as

$$p_{x/y}=\frac{e}{2}\left(\sum_n 2p^n_{x/y} \bmod 2\right), \tag{2}$$

$$q_{xy}=\frac{e}{2}\left(\sum_n 2p^n_x p^n_y \bmod 2\right). \tag{3}$$

Here, $p^n_{x/y}=q^n_{x/y}/2$, with $q^n_{x/y}$ fulfilling the equation $(-1)^{q^n_{x/y}}=\eta^n(M)/\eta^n(\Gamma)$. $\eta^n(M/\Gamma)$ denotes the nth band's eigenvalue of $\hat{C}_{4z}\hat{P}$ at the M/Γ point with $\eta=\xi e^{\pm i\pi/4}$. Note that $p_x=p_y$ due to $\hat{C}_{4z}\hat{P}$ symmetry, and the summation is over all the occupied bands. The 22 (11 pairs) eigenvalues of $\hat{C}_{4z}\hat{P}$ symmetry at the M/Γ point are listed in Tables I and II in Appendix C. Then, $(p_x,p_y)=0$, and $q_{xy}=e/2$. This supports a 2D SOTI in monolayer Néel AFM FeSe/GdClO.

From the generalized bulk-boundary correspondence, a 2D SOTI enables the existence of zero-dimensional corner modes. Figure 2(a) shows a typical cluster of monolayer Néel AFM FeSe. It has two kinds of corners formed by two edges with the same and opposite FM orders. The existence of corner modes can be understood under the following sublattice-chirality-kink picture. From the edge spectrum in Figs. 2(c) and 2(e), two spatially separated one-dimensional massive Dirac bands at two parallel x or y edges can be

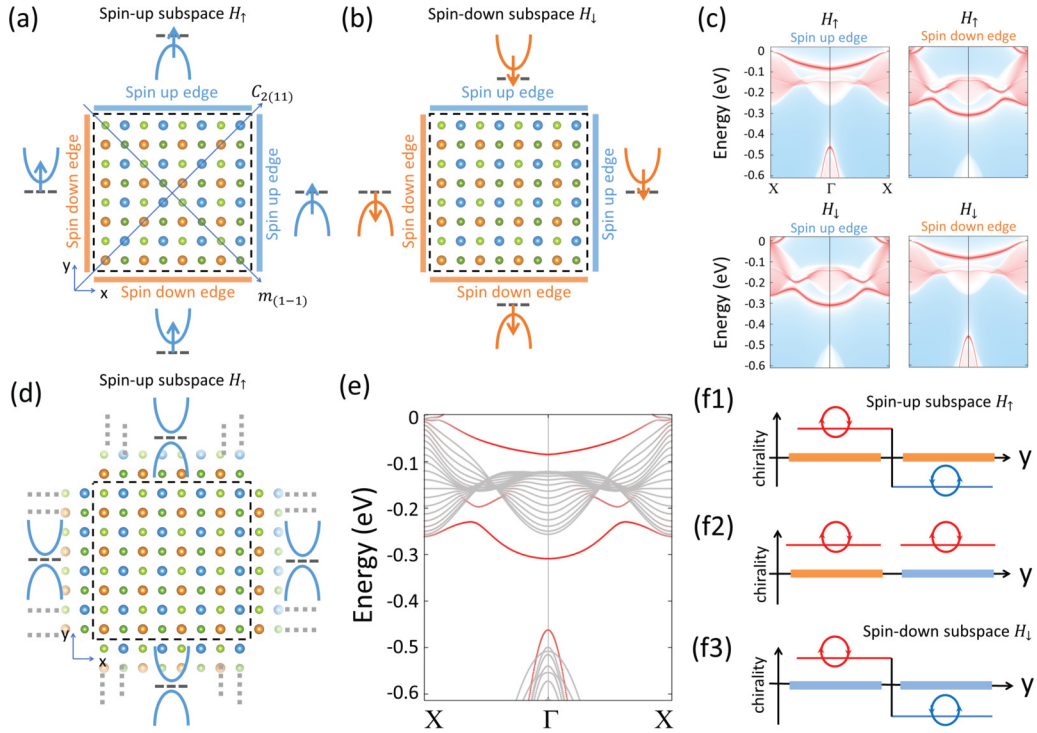

FIG. 2. (a) and (b) Illustration of a monolayer Néel AFM FeSe cluster with a size of 4×4 in units of the unit cells shown in Fig. 1(b). (c) The edge spectrum of spin-up and -down Hamiltonians $H_\uparrow$ and $H_\downarrow$, respectively. The relevant spin-polarized half massive Dirac bands are schematically plotted near four edges of the cluster in (a) and (b). (d) The full massive Dirac bands can be obtained by sticking two parallel edges corresponding to (a). (e) The full edge spectrum without the spin-resolved property. (f1)–(f3) Three kinds of sublattice chirality kinks for three types of corners in (a) and (b).

recombined by sticking two parallel edges together in each spin polarization subspace, as shown in Figs. 2(a) and 2(d). Then, low-energy effective Hamiltonians to describe the edge spectrum can be expressed as

$$H_{\uparrow,x/y}(k_{x/y}) = \pm v k_{x/y} \tau_{y/x} + m\tau_z, \tag{4}$$

$$H_{\downarrow,x/y}(k_{x/y}) = \pm v k_{x/y} \tau_{y/x} - m\tau_z. \tag{5}$$

Here, v is an effective velocity. $k_{x/y}$ are momenta along the x/y direction, and $\tau_{x/y/z}$ are three Pauli matrices defined in sublattice space with intertwined orbital degrees of freedom. m is the mass induced by the AFM order. Note that the effective Hamiltonians in Eqs. (4) and (5) involving the quadratic terms of k can well capture the edge spectrum shown in Fig. 7 in Appendix D. The cluster in Fig. 2(a) has $\hat{P}\hat{T}$, $\hat{C}_{2(1,1)}\hat{T}$, and $\hat{m}_{(1,1)}$ symmetries and two different corners formed by intersections of two of the same and opposite FM edges. Note that $\hat{C}_{2(1,1)}\hat{T}$ builds an intra-spin-subspace connection, and $\hat{P}\hat{T}$ and $\hat{m}_{(1,1)}$ construct an inter-spin-subspace connection. Considering the orbital weight of bulk bands near E_F in Fig. 1(e), the basis functions of the Hamiltonians in Eqs. (4) and (5) can be defined as $\psi_\uparrow(k) = [d_{A,z^2,\uparrow}(k), d_{B,xz+iyz,\uparrow}(k)]^T$ [32,33] and $\psi_\downarrow = \hat{P}\hat{T}\psi_\uparrow(k)$ (see Fig. 6 in Appendix B). Then, the representation matrix U of $\hat{C}_{2(1,1)}\hat{T}$ is $\frac{1}{2}[(1+\tau_z) - i(1-\tau_z)]\mathcal{K}$, with $\mathcal{K}$ being the complex conjugate. For instance, in spin-up subspace, $UH_{\uparrow,x}(k_x)U^\dagger|_{k_x \to -k_y} = v k_y \tau_x + m\tau_z$. In comparison with $H_{\uparrow,y}(k_y)$, the sublattice chirality defined by $\vec{k} \times \vec{\tau}$ changes sign. Namely, there exists a sublattice-chirality kink, as shown in Fig. 2(f1). Thus, a corner mode must appear for the corner formed by two of the same FM edges [49]. However, for the corner formed by two opposite FM edges, $H_{\uparrow,x}(k_x) \xrightarrow{\hat{m}_{(1,1)}} H_{\downarrow,y}(k_y) \xrightarrow{\hat{P}\hat{T}} H_{\uparrow,y}(k_y)$. Namely, two edge Hamiltonians are identical under $\hat{m}_{(1,1)}$ in the restricted $H_\uparrow(k)$ subspace, as shown in Fig. 2(f2). Thus, no zero mode will emerge. Similarly, in spin-down subspace, another corner mode appears from the sublattice-chirality-kink picture, as shown in Fig. 2(f3). Figure 3(a) gives the spectrum of the cluster. One can find two degenerate corner modes located on two corners of two of the same FM edges. Clusters with other patterns are shown Fig. 8 in Appendix E. Note that corner modes are robust against SOC and in-plane magnetic field (see Figs. 9 and 10 in Appendix F). Different from the robustness of topological boundary states in conventional topological insulators, the corner modes in 2D SOTIs depend on the details of the patterns of the clusters (see Fig. 8 in Appendix E). Thus, the role of crystalline symmetry is subtle. The 2D SOTI can be intrinsic if four edges are globally considered and $\hat{C}_{2(1,1)}\hat{T}$ is enforced. Otherwise, the 2D SOTI can be extrinsic if two edges are considered locally [6,50,51]. In any case, two FM edges connected by $\hat{C}_{2(1,1)}\hat{T}$ are the key to enabling the appearance of corner modes.

Different from previous proposals, the above spin-dependent sublattice-chirality-kink picture indicates the FM corner modes should also be spin dependent. Figures 3(b) and 3(c) give the spin-dependent spectrum and distribution of the spin-polarized corner modes. The location of the corner

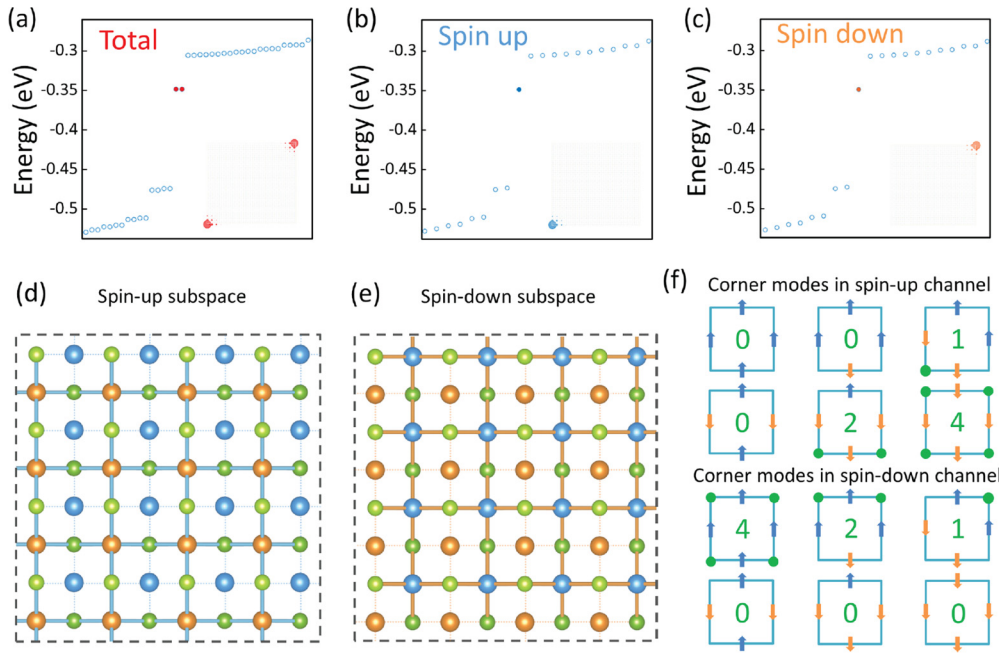

FIG. 3. The discrete energy spectrum of the cluster in Fig. 2(a) without SOC for (a) non-spin-resolved case and (b) and (c) for spin-dependent cases. The insets in (a)–(c) give the density distribution of the corner modes. The cluster size is 20×20 in the calculations. (d) and (e) The relative hopping integral patterns between Fe $xz/yz/z^2$ and the Se z orbital for two spin-decoupled Hamiltonians without SOC, respectively. The strong and weak hoppings are labeled by thick and thin connections, respectively. (f) Summary of the distribution of corner modes with definite spin-up and -down polarization in several different of clusters.

modes can be understood from Figs. 3(d) and 3(e), where the strong and weak hopping integrals are schematically plotted in spin-up and -down subspaces, respectively (see Fig. 11 in Appendix F). The strong bonds of iron atoms in the bottom left and top right corners are broken in spin-up and -down subspaces, respectively. This leaves the relevant corners with isolated spin-dependent corner modes in Figs. 3(b)–3(e). Note that the fidelity of spin polarization is 99.6% with SOC because the spin-dependent nature is governed by magnetic splitting with an energy scale of 2.5 eV in comparison to the tiny SOC energy ~ 0.03 eV. This indicates the spin-dependent feature is robust against other weak external perturbations and enables one to manipulate the spin degree of freedom of corner modes in possible applications. In Fig. 3(f), we give various possibilities to realize corner modes in two spin channels.

The FeSe/GdClO cluster can have distinct AFM edges, as shown in Fig. 4(a). Figures 4(b) and 4(c) give the relevant edge spectra. The remarkable feature is the emergence of two nearly flat bands near $E_F \sim -0.35$ eV. Their formation can be understood according to Fig. 4(d), in which the strong and weak hopping integrals are labeled in spin-up and -down subspaces, respectively. Then, each spin-down and -up iron atom with broken strong bonds can bind a corner mode, as shown in the top and bottom panels in Fig. 4(d), respectively. The isolated corner modes arrange into a one-dimensional array and have weak coupling, forming two degenerate flat bands, as shown in Fig. 4(b). SOC can further induce weak coupling to break the degeneracy of flat bands, as shown in Fig. 4(c). Numerical calculations for a square cluster with four AFM edges indicate four different AFM corner modes with each of the four quadruple degeneracies exist, as shown in Fig. 4(f). The AFM corner modes have lower energy than the bottom of the flat bands. This indicates the general kink picture is violated. Interestingly, we find that AFM corner modes can be understood by following the one-dimensional Schrodinger equation by considering the edge mapping shown in Fig. 4(e),

$$H_{\mathrm{AFM}}(k \to -i\partial_x)\psi(x) = E\psi(x), \tag{6}$$

with

$$H_{\mathrm{AFM}}(k \to -i\partial_x) = -\frac{\hbar^2}{2m^*}\frac{d^2}{dx^2} + V(x). \tag{7}$$

Here, m^* is the effective mass of the flat bands. $V(x)$ is the effective potential well near a corner of two AFM edges. $V(x)$ can be approximately expressed by a square potential well. $V(x) = -V_i$ when $|x| < a/2$, and otherwise, $V(x) = 0$. Here, a denotes the width of the potential. i is 1 or 2, labeling two different flat bands. The bound-state solutions of Eq. (6) are standard. The even-parity solution is $E_{i,n} = \frac{\pi^2\hbar^2}{2m^*a^2}(2n+1)^2 - V_i$ and $\psi_n(x) \sim \cos k_n x$ for $|x| < a/2$ and $\sim e^{-\alpha_n|x|}$ for $|x| > a/2$. The odd-parity solution is $E_{i,n} = \frac{\pi^2\hbar^2}{2m^*a^2}(2n+2)^2 - V_i$ and $\psi_n(x) \sim \sin k_n x$ for $|x| < a/2$ and $\sim e^{-\alpha_n|x|}$ for $|x| > a/2$. n takes values of 0, 1, 2, ... The numerical results in Fig. 4(f) indicate the four different emergent corner modes correspond to $E_{1,0}$, $E_{2,0}$, $E_{1,1}$, $E_{2,1}$, with consistent even and odd alternating distribution patterns, as shown in Figs. 4(f)–4(i). It seems that the AFM corner modes are not topologically protected. However, their emergence can be traced back to the FM corner modes. Thus, both FM and AFM corner modes are topologically protected in a different hierarchical manner. Note that at least one AFM corner mode exists for any $V(x)$ well.

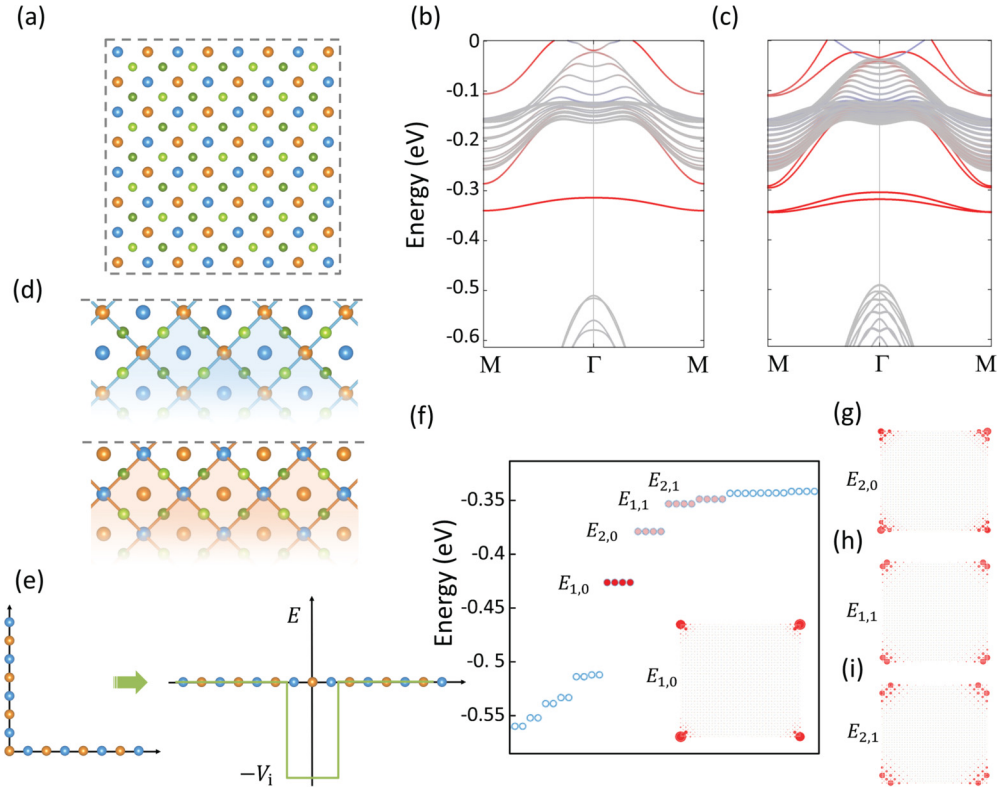

FIG. 4. (a) A cluster of monolayer FeSe with a size of 4 × 4 in units of the $\sqrt{2}$ unit cell shown in Fig. 1(b). The cluster size is 14 × 14 in the calculations in (e)–(h). (b) and (c) The AFM edge spectrum without SOC and with SOC, respectively. (d) The relative hopping integral patterns for decoupled spin-up (top panel) and -down (bottom panel) Hamiltonians without SOC. (e) The mapping of two AFM edges from the orthogonal to linear configuration. (f) The discrete energy spectrum corresponds to (a). The inset gives the density distribution of the corner mode with four-quadruple degeneracy and the lowest energy. (f)–(h) The density distributions of the other three corner modes with increasing energy.

III. DISCUSSIONS AND CONCLUSIONS

In many previous proposals, in-plane external magnetic field or the magnetic proximity effect was induced to drive 2D SOTIs. Corner modes are sensitive to these fine tunings. They increase the difficulty of constructing electronic devices based on corner modes. The 2D SOTI and relevant corner modes here are robust against in-plane external magnetic field and other perturbations (see also Figs. 10 and 12 in Appendix F). The corner modes here lie 0.35 eV below the original Fermi energy. To experimentally detect them, scanning tunneling spectroscopy is a feasible technique because it can measure the spin-resolved local density of states by changing the voltage in a large regime. The transport properties of the corner modes can be studied only when their energy is tuned to the Fermi level. Such tuning can be experimentally realized by electrostatic gating or proton gating techniques, both of which are mature and have special advantages in layered heterostructures [52–54]. In particular, such gated tuning has been realized in FeSe thin flakes [55–57]. Once appropriate hole carriers are induced by gating to change corner mode energy to Fermi energy, monolayer FeSe/GdClO could be an ideal platform to study the properties of 2D SOTIs and relevant corner modes.

In conclusion, we proposed that a monolayer FeSe/GdClO heterostructure can realize a 2D second-order topological insulator which is free from SOC and in-plane magnetic field. Furthermore, we found that corner modes are protected by a large gap of about 0.3 eV and can be detected at high temperature. We also found two distinct types of FM and AFM corner modes exist. More interestingly, we showed that FM corner modes follow a sublattice-chirality-kink picture and have a unique spin-dependent property and AFM corner modes emerge from the FM corner mode array. The diversity of FM and AFM corner modes provides a way to construct relevant devices by utilizing their spin degree of freedom.

ACKNOWLEDGMENTS

We thank L. Hao for helpful discussions. This work was financially supported by the National Key R&D Program of China (Grants No. 2022YFA1403200 and No. 2017YFA0303201), the National Natural Science Foundation of China (Grants No. 92265104, No. 12022413, and No. 11674331), the "Strategic Priority Research Program (B)" of the Chinese Academy of Sciences (Grant No. XDB33030100), the Collaborative Innovation Program of Hefei Science Center, CAS (Grant No. 2020HSC-CIP002), and the Major Basic Program of Natural Science Foundation of Shandong Province (Grant No. ZR2021ZD01). A portion of this work was supported by the High Magnetic Field Laboratory of Anhui Province, China. A portion of the numerical

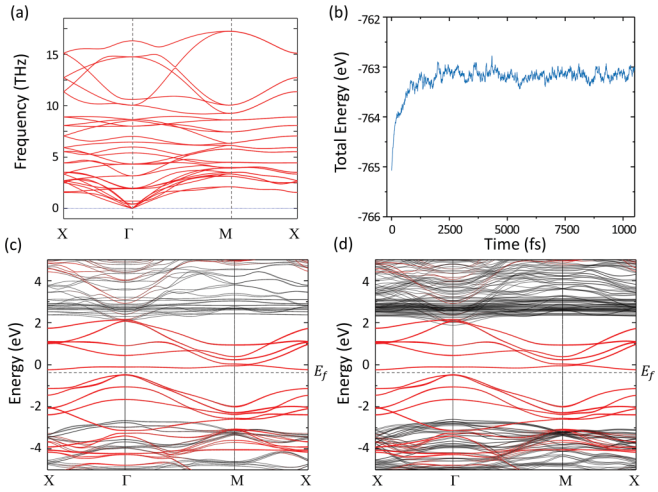

FIG. 5. (a) The phonon spectrum of a monolayer FeSe/GdClO heterostructure. (b) The AIMD evolutions of total energy at 300 K for the monolayer FeSe/GdClO heterostructure. (c) The total band structure of a FeSe/GdClO heterostructure on monolayer substrates. (d) The total band structure of a FeSe/GdClO heterostructure on multilayer substrates.

computations was performed at the Hefei Advanced Computing Center.

APPENDIX A: FIRST-PRINCIPLES CALCULATIONS METHOD

In this and the following Appendixes, we give the details of the first-principles calculation method, a clarification of the stability and magnetism of the heterostructure, cases for clusters with other patterns, and numerical evidence of the robustness of the HOTI and corner modes against perturbations, including SOC, in-plane magnetic field, etc.

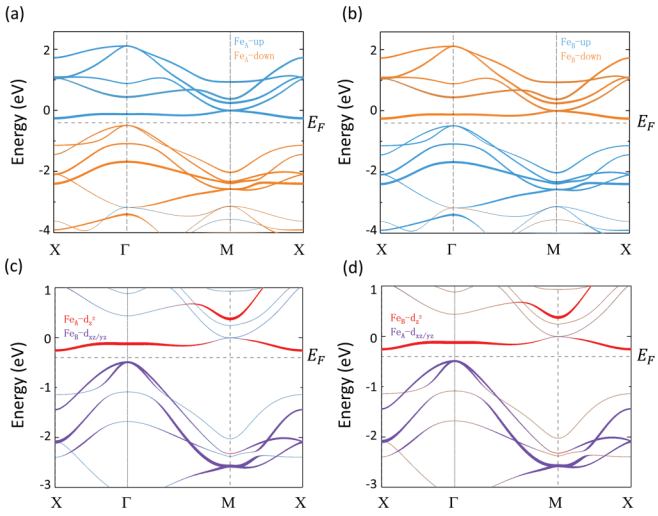

FIG. 6. (a) and (b) Spin-polarized band structures of the A and B sublattices of Fe atoms in the monolayer Néel AFM FeSe, respectively. (c) and (d) For the spin-up/-down-polarized band structure of the monolayer Néel AFM FeSe, the weights of the d_{z^2} orbitals of sublattice A/B and the $d_{xz/yz}$ orbitals of sublattice B/A are shown in red and purple, respectively.

TABLE I. The 11 ξ values calculated at points Γ and M. From left to right, the ξ values are sorted from the lowest to the highest occupied band.

	ξ
Γ	$+1, -1, +1, -1, -1, +1, -1, +1, -1, -1, +1$
M	$-1, -1, -1, +1, +1, +1, -1, +1, +1, +1, -1$

The first-principles calculations based on density functional theory (DFT) were carried out using the Vienna Ab initio Simulation Package (VASP) program [58] with the generalized gradient approximation with the Perdew-Burke-Ernzerhof functional (PBE) [59]. A vacuum layer 20 Å thick was used to ensure decoupling between neighboring slabs, and the vdW corrections were included using the density functional theory including dispersion correction (DFT-D3) method in our calculations of the monolayer FeSe/GdClO heterostructure [60]. All atoms were fully relaxed until the forces on each atoms were smaller than 0.01 eV/Å in heterostructure relaxations. We adopted the PBE + U calculation method to deal with the $3d$ orbitals of Fe with $U_{\text{eff}} = 0.5$ eV and the $4f$ orbitals of Gd with $U_{\text{eff}} = 5$ eV. The first-principles-based tight-binding Hamiltonian with 32 Wannier orbits of AFM FeSe was obtained from the band fitting by using the WANNIER90 package [61].

APPENDIX B: STABILITY, BAND DECOUPLING, AND MAGNETIC CONFIGURATION OF THE FeSe/GdClO HETEROSTRUCTURE

For the stability of the FeSe/GdClO heterostructure, we calculated the phonon spectrum. The result is shown in Fig. 5(a). We can see that the no imaginary frequency appears. We further performed *ab initio* molecular dynamics (AIMD) simulations at 300 K for 10 ps, as shown in Fig. 5(b). The results show that the FeSe/GdClO heterostructure possesses both thermal and dynamical stability. Figure 5(c) shows that the electronic states are nearly decoupled between monolayer FeSe and the monolayer GdClO substrate. For comparison, we constructed a heterostructure with three layers of the GdClO substrate, which has 15 layers of atoms and is about

TABLE II. The 22 η values calculated at points Γ and M. From left to right, the η values are sorted from the lowest to the highest occupied band.

	η
Γ	$\{e^{i\pi/4}, e^{-i\pi/4}\}, \{-e^{i\pi/4}, -e^{-i\pi/4}\}, \{e^{i\pi/4}, e^{-i\pi/4}\},$ $\{-e^{i\pi/4}, -e^{-i\pi/4}\}, \{-e^{i\pi/4}, -e^{-i\pi/4}\}, \{e^{i\pi/4}, e^{-i\pi/4}\},$ $\{-e^{i\pi/4}, -e^{-i\pi/4}\}, \{e^{i\pi/4}, e^{-i\pi/4}\}, \{-e^{i\pi/4}, -e^{-i\pi/4}\},$ $\{-e^{i\pi/4}, -e^{-i\pi/4}\}, \{e^{i\pi/4}, e^{-i\pi/4}\}$
M	$\{-e^{i\pi/4}, -e^{-i\pi/4}\}, \{-e^{i\pi/4}, -e^{-i\pi/4}\}, \{-e^{i\pi/4}, -e^{-i\pi/4}\},$ $\{e^{i\pi/4}, e^{-i\pi/4}\}, \{e^{i\pi/4}, e^{-i\pi/4}\}, \{e^{i\pi/4}, e^{-i\pi/4}\},$ $\{-e^{i\pi/4}, -e^{-i\pi/4}\}, \{e^{i\pi/4}, e^{-i\pi/4}\}, \{e^{i\pi/4}, e^{-i\pi/4}\},$ $\{e^{i\pi/4}, e^{-i\pi/4}\}, \{-e^{i\pi/4}, -e^{-i\pi/4}\}$

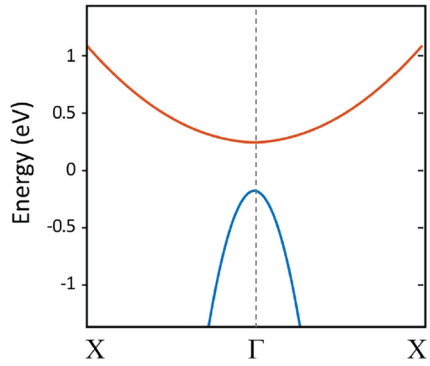

FIG. 7. The modified low-energy effective Hamiltonian energy spectrum. We have set $\alpha = -0.8$, $\beta = 1$, $\upsilon = 0.4$, and $m = 0.2$.

20 Å thick. As shown in Fig. 5(d), the band structures of the FeSe/GdClO heterostructure on monolayer and multilayer substrates indicate that the band structures of FeSe and GdClO remained almost decoupled. The spin-polarized band structures of monolayer Néel AFM FeSe are shown in Fig. 6.

The A sublattice of the Fe square lattices can generate ferromagnetism with the aid of the top layer of Gd. Therefore, the different magnetism of the B sublattice of the Fe square lattices will form the different monolayer FeSe magnetic configuration. For different magnetic configurations of FeSe in a monolayer FeSe/GdClO heterostructure, the total energy of AFM-FeSe is 609 meV lower than that of FM-FeSe, $E_{\mathrm{AFM}} - E_{\mathrm{FM}} = -609$ meV, which indicates that the antiferromagnetic configuration of FeSe in a monolayer FeSe/GdClO heterostructure is more stable. In addition, we also performed a self-consistent calculation without setting the magnetic moment on the B sublattice of the Fe square lattices initially, and the results show that it will spontaneously form in the opposite polarization of the A sublattice of the Fe square lattices.

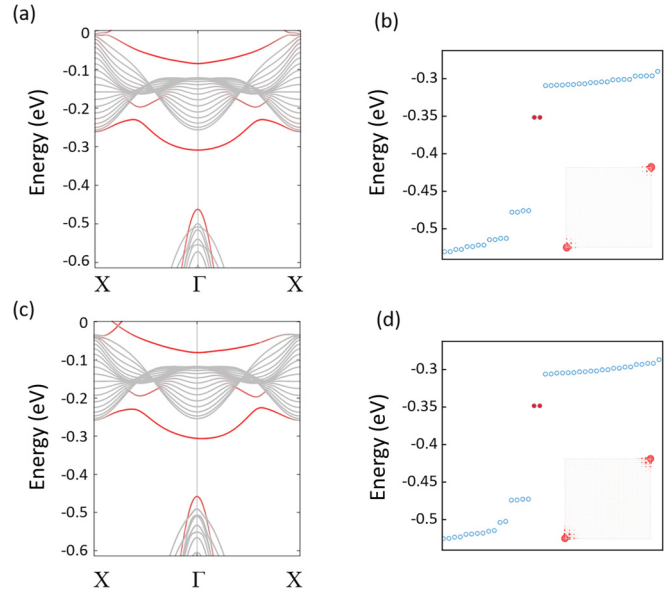

FIG. 9. The FM edge spectrum and discrete energy spectrum of the cluster with a size of 20 × 20 unit cells (a) and (b) without SOC and (c) and (d) with SOC, respectively. The red circles in (b) and (d) correspond to the corner modes.

APPENDIX C: TOPOLOGICAL CHARACTERIZATION OF THE SOTI

The ξ and η values in Eqs. (1)–(3) at points Γ and M are listed in Tables I and II.

APPENDIX D: MODIFIED LOW-ENERGY EFFECTIVE HAMILTONIAN

The low-energy effective Hamiltonian model is presented to directly reflect which combination of different edge spectra can produce the sublattice-chirality-kink picture to generate spin-dependent corner modes. In order to further capture the shape of the edge spectrum obtained from the DFT shown in

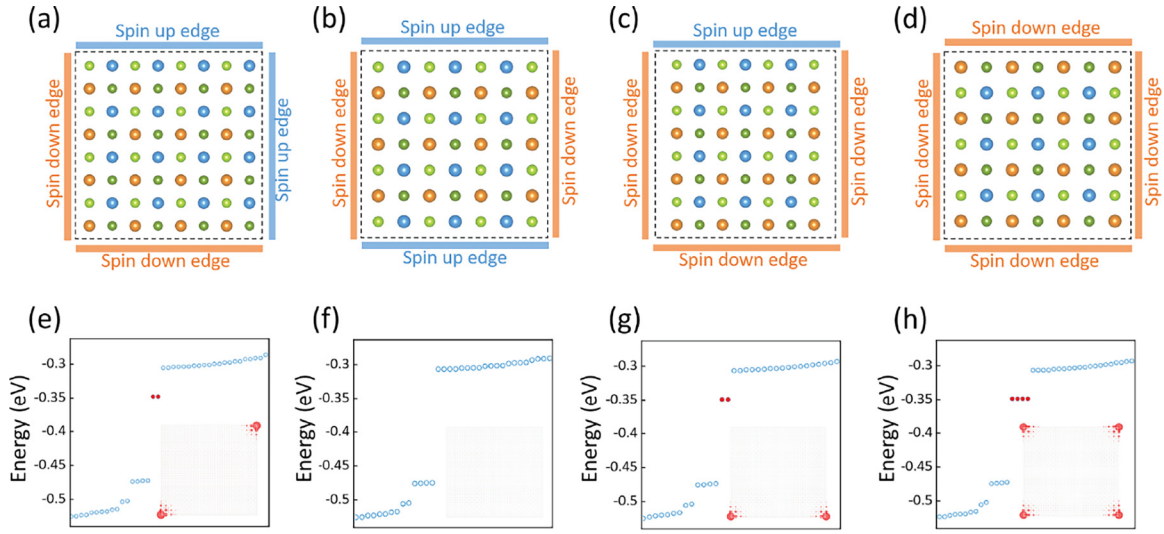

FIG. 8. (a)–(d) Different patterns of the monolayer Néel AFM FeSe cluster with a size of 20 × 20 and four FM edges. (e)–(h) The discrete energy spectrum of the clusters in (a)–(d), respectively. The red circles in (e)–(h) correspond to the corner modes. The insets in (e)–(h) give the density distribution of the corner modes.

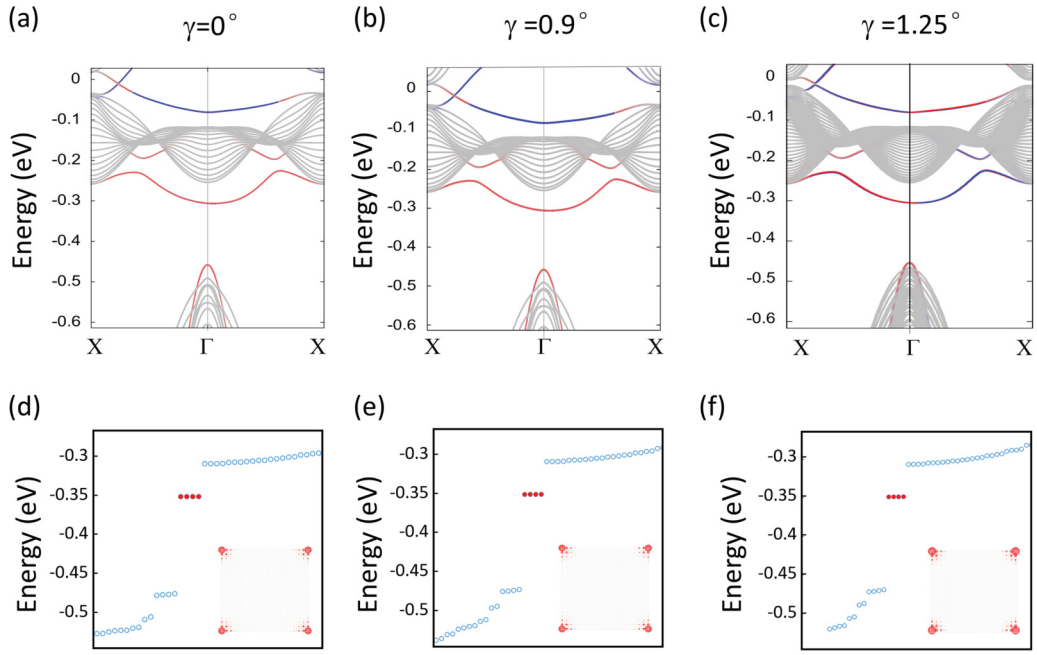

FIG. 10. Effect of in-plane magnetic field on corner modes of the monolayer Néel AFM FeSe cluster. γ represents the angle of the tilt of the magnetic moment from the vertical direction caused by the in-plane magnetic field, which is used to represent the magnitude of the in-plane magnetic field. (a)–(c) The FM edge spectrum of the monolayer Néel AFM FeSe cluster with increasing in-plane magnetic field. (d)–(f) The discrete energy spectrum of the cluster.

Fig. 2(e), the modified low-energy effective Hamiltonians can be expressed as

$$H_{\uparrow,x/y}(k_{x/y}) = \alpha k_{x/y}^2 \pm v k_{x/y}\tau_{y/x} + \left(m + \beta k_{x/y}^2\right)\tau_z, \quad \text{(D1)}$$

$$H_{\downarrow,x/y}(k_{x/y}) = \alpha k_{x/y}^2 \pm v k_{x/y}\tau_{y/x} - \left(m + \beta k_{x/y}^2\right)\tau_z. \quad \text{(D2)}$$

Here, the addition of two quadratic terms gives the energy spectrum a quadratic shape. The first quadratic term is used to break the particle-hole symmetry. Note that the addition of two quadratic terms has no effect on the sublattice-chirality-kink picture. The modified low-energy effective Hamiltonian energy spectrum is shown in Fig. 7, where it can be seen that the shape of the edge spectrum shown in Fig. 2(e) can be captured with appropriate parameters.

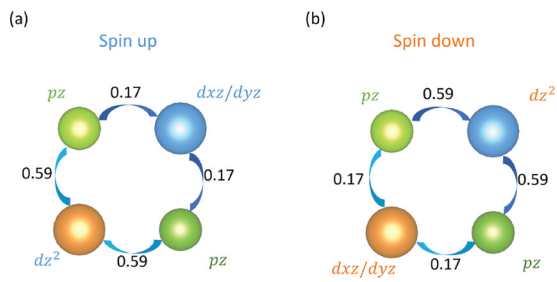

FIG. 11. (a) and (b) The relative hopping integral between different atomic orbits for decoupled spin-up and spin-down Hamiltonians without SOC, respectively.

APPENDIX E: DIFFERENT PATTERNS OF THE MONOLAYER NÉEL AFM FeSe CLUSTER

From the sublattice-chirality-kink picture, we proved that a corner mode must appear for the corner formed by two of the same FM edges. Here, we list all possible nonequivalent

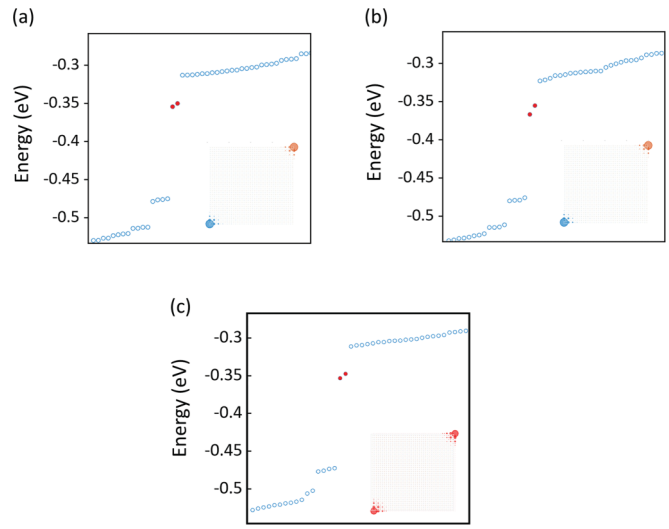

FIG. 12. (a) and (b) The discrete energy spectrum of the monolayer Néel AFM FeSe cluster with disorder effects in the energy ranges of ±10 and ±50 meV, respectively. The insets in (a) and (b) give the density distribution of the corner modes. (c) Some perturbations are added to simulate the effect of unequal magnetic moments or some impurity defects on corner modes of the monolayer Néel AFM FeSe cluster.

patterns of the monolayer Néel AFM FeSe cluster. All four different cluster patterns are shown in Fig. 8(a)–8(d). We can see that the number of corner modes and the density distributions of the corner modes appear to be very different for different cluster patterns.

APPENDIX F: THE ROBUSTNESS OF THE SPIN-DEPENDENT CORNER MODE

Considering SOC, we calculated the edge spectrum and discrete energy spectrum of the cluster with the patterns in Fig. 8(a), and the results are shown in Fig. 9. We find that the two corner states remain degenerate. Similarly, we introduced the in-plane magnetic field and calculated the edge spectrum and discrete energy spectrum of the cluster with the pattern in Fig. 8(d), and the results are shown in Fig. 10. The strong and weak hopping integral patterns between different atomic orbits for decoupled spin-up and down channels are shown in Fig. 11. The above results indicate that the corner modes are robust against SOC and in-plane magnetic field. In addition, we further consider the influence of different degrees of disorder effect and some perturbations on the stability of spin-dependent corner modes of the monolayer Néel AFM FeSe cluster; as shown in Fig. 12, the corner modes still exist stably, which is beneficial for possible subsequent experimental measurements.

[1] W. A. Benalcazar, B. A. Bernevig, and T. L. Hughes, Electric multipole moments, topological multipole moment pumping, and chiral hinge states in crystalline insulators, Phys. Rev. B **96**, 245115 (2017).

[2] W. A. Benalcazar, B. A. Bernevig, and T. L. Hughes, Quantized electric multipole insulators, Science **357**, 61 (2017).

[3] Z. Song, Z. Fang, and C. Fang, $(d-2)$-Dimensional Edge States of Rotation Symmetry Protected Topological States, Phys. Rev. Lett. **119**, 246402 (2017).

[4] F. Schindler, A. M. Cook, M. G. Vergniory, Z. Wang, S. S. P. Parkin, B. A. Bernevig, and T. Neupert, Higher-order topological insulators, Sci. Adv. **4**, eaat0346 (2018).

[5] G. van Miert and C. Ortix, Higher-order topological insulators protected by inversion and rotoinversion symmetries, Phys. Rev. B **98**, 081110 (2018).

[6] E. Khalaf, Higher-order topological insulators and superconductors protected by inversion symmetry, Phys. Rev. B **97**, 205136 (2018).

[7] M. Geier, L. Trifunovic, M. Hoskam, and P. W. Brouwer, Second-order topological insulators and superconductors with an order-two crystalline symmetry, Phys. Rev. B **97**, 205135 (2018).

[8] D. Călugăru, V. Juričić, and B. Roy, Higher-order topological phases: A general principle of construction, Phys. Rev. B **99**, 041301 (2019).

[9] Y. Ren, Z. Qiao, and Q. Niu, Engineering Corner States from Two-Dimensional Topological Insulators, Phys. Rev. Lett. **124**, 166804 (2020).

[10] C.-A. Li and S.-S. Wu, Topological states in generalized electric quadrupole insulators, Phys. Rev. B **101**, 195309 (2020).

[11] Y.-B. Yang, K. Li, L.-M. Duan, and Y. Xu, Type-II quadrupole topological insulators, Phys. Rev. Res. **2**, 033029 (2020).

[12] M. Jung, Y. Yu, and G. Shvets, Exact higher-order bulk-boundary correspondence of corner-localized states, Phys. Rev. B **104**, 195437 (2021).

[13] S. Mittal, V. V. Orre, G. Zhu, M. A. Gorlach, A. Poddubny, and M. Hafezi, Photonic quadrupole topological phases, Nat. Photonics **13**, 692 (2019).

[14] L. He, Z. Addison, E. J. Mele, and B. Zhen, Quadrupole topological photonic crystals, Nat. Commun. **11**, 3119 (2020).

[15] M. Serra-Garcia, V. Peri, R. Susstrunk, O. R. Bilal, T. Larsen, L. G. Villanueva, and S. D. Huber, Observation of a phononic quadrupole topological insulator, Nature (London) **555**, 342 (2018).

[16] Y. Qi, C. Qiu, M. Xiao, H. He, M. Ke, and Z. Liu, Acoustic Realization of Quadrupole Topological Insulators, Phys. Rev. Lett. **124**, 206601 (2020).

[17] C. W. Peterson, W. A. Benalcazar, T. L. Hughes, and G. Bahl, A quantized microwave quadrupole insulator with topologically protected corner states, Nature (London) **555**, 346 (2018).

[18] S. Imhof, C. Berger, F. Bayer, J. Brehm, L. W. Molenkamp, T. Kiessling, F. Schindler, C. H. Lee, M. Greiter, T. Neupert, and R. Thomale, Topolectricalcircuit realization of topological corner modes, Nat. Phys. **14**, 925 (2018).

[19] M. Serra-Garcia, R. Susstrunk, and S. D. Huber, Observation of quadrupole transitions and edge mode topology in an LC circuit network, Phys. Rev. B **99**, 020304 (2019).

[20] E. Lee, R. Kim, J. Ahn, and B. Yang, Two-dimensional higher-order topology in monolayer graphdiyne, npj Quantum Mater. **5**, 1 (2020).

[21] X. Sheng, C. Chen, H. Liu, Z. Chen, Z. Yu, Y. X. Zhao, and S. A. Yang, Two-Dimensional Second-Order Topological Insulator in Graphdiyne, Phys. Rev. Lett. **123**, 256402 (2019).

[22] B. Liu, G. Zhao, Z. Liu, and Z. F. Wang, Two-dimensional quadrupole topological insulator in γ-graphyne, Nano Lett. **19**, 6492 (2019).

[23] M. Park, Y. Kim, G. Cho, and S. B. Lee, Higher-Order Topological Insulator in Twisted Bilayer Graphene, Phys. Rev. Lett. **123**, 216803 (2019).

[24] C. Ma, Q. Wang, S. Mills, X. Chen, B. Deng, S. Yuan, C. Li, K. Watanabe, T. Taniguchi, X. Du, F. Zhang, and F. Xia, Moiré band topology in twisted bilayer graphene, Nano Lett. **20**, 6076 (2020).

[25] B. Liu, L. Xian, H. Mu, G. Zhao, Z. Liu, A. Rubio, and Z. F. Wang, Higher-Order Band Topology in Twisted Moiré Superlattice, Phys. Rev. Lett. **126**, 066401 (2021).

[26] C. Chen, Z. Song, J. Zhao, Z. Chen, Z. Yu, X. Sheng, and S. A. Yang, Universal Approach to Magnetic Second-Order Topological Insulator, Phys. Rev. Lett. **125**, 056402 (2020).

[27] Q. Y. Wang, Z. Li, W. H. Zhang, Z. C. Zhang, J. S. Zhang, W. Li, H. Ding, Y. B. Ou, P. Deng, K. Chang, J. Wen, C. Song, K. He, J. Jia, S. Ji, Y. Wang, L. Wang, X. Chen, X. Ma, and Q. Xue, Interface induced high temperature superconductivity in single unit-cell FeSe films on $SrTiO_3$, Chin. Phys. Lett. **29**, 037402 (2012).

[28] R. Peng, H. C. Xu, S. Y. Tan, H. Y. Cao, M. Xia, X. P. Shen, Z. C. Huang, C. H. P. Wen, Q. Song, T. Zhang, B. P. Xie, X. G. Gong, and D. L. Feng, Tuning the band structure and

superconductivity in single-layer FeSe by interface engineering, Nat. Commun. **5**, 5044 (2014).

[29] J. Shiogai, Y. Ito, T. Mitsuhashi, T. Nojima, and A. Tsukazaki, Electric-field-induced superconductivity in electrochemically etched ultrathin FeSe films on $SrTiO_3$ and MgO, Nat. Phys. **12**, 42 (2016).

[30] H. Ding, Y. Lv, K. Zhao, W. Wang, L. Wang, C. Song, X. Chen, X. Ma, and Q. Xue, High-Temperature Superconductivity in Single-Unit-Cell FeSe Films on Anatase TiO_2(001), Phys. Rev. Lett. **117**, 067001 (2016).

[31] C. Liu, H. Shin, A. Doll, H. Kung, Ryan P. Day, B. A. Davidson, J. Dreiser, G. Levy, A. Damascelli, C. Piamonteze, and K. Zou, High-temperature superconductivity and its robustness against magnetic polarization in monolayer FeSe on $EuTiO_3$, npj Quantum Mater. **6**, 85 (2021).

[32] N. Hao and J. Hu, Topological Phases in the Single-Layer FeSe, Phys. Rev. X **4**, 031053 (2014).

[33] N. Hao and J. Hu, Topological quantum states of matter in iron-based superconductors: From concept to material realization, Natl. Sci. Rev. **6**, 213 (2019).

[34] Z. F. Wang, H. Zhang, D. Liu, C. Liu, C. Tang, C. Song, Y. Zhong, J. Peng, F. Li, C. Nie, L. Wang, X. Zhou, X. Ma, Q. Xue, and F. Liu, Topological edge states in a high-temperature superconductor FeSe/$SrTiO_3$(001) film, Nat. Mater. **15**, 968 (2016).

[35] F. Zheng, Z. Wang, W. Kang, and P. Zhang, Antiferromagnetic FeSe monolayer on $SrTiO_3$: The charge doping and electric field effects, Sci. Rep. **3**, 2213 (2013).

[36] K. Liu, Z. Lu, and T. Xiang, Atomic and electronic structures of FeSe monolayer and bilayer thin films on $SrTiO_3$ (001): First-principles study, Phys. Rev. B **85**, 235123 (2012)

[37] H. Cao, S. Chen, H. Xiang, and X. Gong, Antiferromagnetic ground state with pair-checkerboard order in FeSe, Phys. Rev. B **91**, 020504(R) (2015).

[38] S. Y. Tan, Y. Zhang, M. Xia, Z. Ye, F. Chen, X. Xie, R. Peng, D. Xu, Q. Fan, H. Xu, J. Jiang, T. Zhang, X. Lai, T. Xiang, J. Hu, B. Xie, and D. Feng, Interface-induced superconductivity and strain-dependent spin density wave in FeSe/$SrTiO_3$ thin films, Nat. Mater. **12**, 634 (2013).

[39] H. Y. Cao, S. Y. Tan, H. J. Xiang, D. L. Feng, and X. G. Gong, Interfacial effects on the spin density wave in FeSe/$SrTiO_3$ thin films, Phys. Rev. B **89**, 014501 (2014).

[40] Y. Zhou, L. Miao, P. Wang, F. F. Zhu, W. X. Jiang, S. W. Jiang, Y. Zhang, B. Lei, X. H. Chen, H. F. Ding, H. Zheng, W. T. Zhang, J.-F. Jia, D. Qian, and D. Wu, Antiferromagnetic Order in Epitaxial FeSe Films on $SrTiO_3$, Phys. Rev. Lett. **120**, 097001 (2018).

[41] Y. Gu, Q. Wang, H. Wo, Z. He, H. C. Walker, J. T. Park, M. Enderle, A. D. Christianson, W. Wang, and J. Zhao, Frustrated magnetic interactions in FeSe, Phys. Rev. B **106**, L060504 (2022).

[42] C. Bungenstock, T. Tröster, W. B. Holzapfel, L. Fini and M. Santoro, Energy levels of Pr^{3+}: GdOCl under pressure, J. Phys.: Condens. Matter **12**, 6959 (2000).

[43] K. R. Kort and S. Banerjee, Oriented Electrophoretic Deposition of GdOCl Nanoplatelets, J. Phys. Chem. B **117**, 1585 (2013).

[44] C. Bungenstock, T. Tröster, and W. B. Holzapfel, Effect of pressure on free-ion and crystal-field parameters of Pr^{3+} in *L*OCl (*L* = La, Pr, Gd), Phys. Rev. B **62**, 7945 (2000).

[45] M. R. Osanloo, M. L. Van de Put, A. Saadat, and W. G. Vandenberghe, Identification of two-dimensional layered dielectrics from first principles, Nat. Commun. **12**, 5051 (2021).

[46] D. Boglaienko, A. Andersenb, S. M. Healdc, T. Vargab, D. R. Mortensend, S. Tetefe, G. T. Seidlere, N. Govindf, and T. G. Levitskaiaa, X-ray absorption spectroscopy of trivalent Eu, Gd, Tb, and Dy chlorides and oxychlorides, J. Alloys Compd. **897**, 162629 (2022).

[47] A. Luo, Z. Song, and G. Xu, Fragile topological band in the checkerboard antiferromagnetic monolayer FeSe, npj Comput. Mater. **8**, 26 (2022).

[48] H. Mu, G. Zhao, H. Zhang, and Z. Wang, Antiferromagnetic second-order topological insulator with fractional mass-kink, npj Comput. Mater. **8**, 82 (2022).

[49] R. Jackiw and C. Rebbi, Solitons with fermion number 1/2, Phys. Rev. D **13**, 3398 (1976).

[50] E. Khalaf, W. A. Benalcazar, T. L. Hughes, and R. Queiroz, Boundary-obstructed topological phases, Phys. Rev. Res. **3**, 013239 (2021).

[51] L. Trifunovic and P. W. Brouwer, Higher-order topological band structures, Phys. Status Solidi B **258**, 2000090 (2021).

[52] J. T. Ye, S. Inoue, K. Kobayashi, Y. Kasahara, H. T. Yuan, H. Shimotani, and Y. Iwasa, Liquid-gated interface superconductivity on an atomically flat film, Nat. Mater. **9**, 125 (2010).

[53] J. T. Ye, Y. J. Zhang, R. Akashi, M. S. Bahramy, R. Arita, and Y. Iwasa, Superconducting dome in a gate-tuned band insulator, Science **338**, 1193 (2012).

[54] D. Costanzo, S. Jo, H. Berger, and A. F. Morpurgo, Gate-induced superconductivity in atomically thin MoS_2 crystals, Nat. Nanotechnol. **11**, 339 (2016).

[55] B. Lei, J. H. Cui, Z. J. Xiang, C. Shang, N. Z. Wang, G. J. Ye, X. G. Luo, T. Wu, Z. Sun, and X. H. Chen, Evolution of High-Temperature Superconductivity from a Low-T_c Phase Tuned by Carrier Concentration in FeSe Thin Flakes, Phys. Rev. Lett. **116**, 077002 (2016).

[56] B. Lei, N. Z. Wang, C. Shang, F. B. Meng, L. K. Ma, X. G. Luo, T. Wu, Z. Sun, Y. Wang, Z. Jiang, B. H. Mao, Z. Liu, Y. J. Yu, Y. B. Zhang, and X. H. Chen, Tuning phase transitions in FeSe thin flakes by field-effect transistor with solid ion conductor as the gate dielectric, Phys. Rev. B **95**, 020503 (2017).

[57] C. S. Zhu, J. H. Cui, B. Lei, N. Z. Wang, C. Shang, F. B. Meng, L. K. Ma, X. G. Luo, T. Wu, Z. Sun, and X. H. Chen, Tuning electronic properties of $FeSe_{0.5}Te_{0.5}$ thin flakes using a solid ion conductor field-effect transistor, Phys. Rev. B **95**, 174513 (2017).

[58] G. Kresse and J. Furthmüller, Efficient iterative schemes for *ab initio* total-energy calculations using a plane-wave basis set, Phys. Rev. B **54**, 11169 (1996).

[59] J. P. Perdew, K. Burke, and M. Ernzerhof, Generalized Gradient Approximation Made Simple, Phys. Rev. Lett. **77**, 3865 (1996).

[60] S. Grimme, J. Antony, S. Ehrlich, and S. Krieg, A consistent and accurate ab initio parametrization of density functional dispersion correction (DFT-D) for the 94 elements H-Pu, J. Chem. Phys. **132**, 154104 (2010).

[61] A. A. Mostofi, J. R. Yates, G. Pizzi, Y. S. Lee, I. Souza, D. Vanderbilt, and N. Marzari, An updated version of wannier90: A tool for obtaining maximally-localised Wannier functions, Comput. Phys. Commun. **185**, 2309 (2014).